Critical Roles of Mechanical Properties of Solid Electrolyte Interphase for Potassium Metal Anodes

Yao Gao [1], *Zhen Hou* [1], *Rui Zhou* [1], *Danni Wang* [1], *Xuyun Guo* [1], *Ye Zhu* [1], *Biao Zhang* [1,2]*

[1] Department of Applied Physics, The Hong Kong Polytechnic University, Hung Hom, Hong Kong, China.

[2] Guangdong-Hong Kong-Macao Joint Laboratory for Photonic-Thermal-Electrical Energy Materials and Devices, Research Institute for Smart Energy, The Hong Kong Polytechnic University, Hong Kong, China

* Correspondence: biao.ap.zhang@polyu.edu.hk

Keywords: low concentration, atomic force microscopy, deformation energy, electric field, dendrite growth

The mechanical properties of solid electrolyte interphase (SEI) have attracted increasing attention, but their importance in guiding electrolyte design remains ambiguous. Here we reveal that, despite a decrease in ionic conductivity for both electrolyte and SEI, exceptional cycling performance of K-metal batteries is achieved in a low concentration carbonate electrolyte by optimizing the mechanical stability of the SEI. The SEI formed in the studied carbonate electrolytes is predominantly organic. Its inorganic content increases with increasing electrolyte concentration and corresponds to an increase in Young's modulus (E) and ionic conductivity of SEI and a decrease in elastic strain limit (ε_{Y}). The maximum elastic deformation energy combines effects of E and ε_{Y}, achieving a maximum in 0.5 M electrolyte. Finite element simulations indicate that SEI with low either E or ε_{Y} inevitably triggers dendrite growth. These findings foreshadow an increased focus on mechanical properties of SEI, where low concentrations of carbonate electrolytes display merit.

1. Introduction

The rational design and innovation of electrolyte systems play a decisive role in advancing battery technology.[1] The interaction between salts and solvent molecules determines electrolyte characteristics, such as ionic conductivity, thermal and electrochemical stabilities.[2] The properties of solid electrolyte interphase (SEI), which is the decomposition product of electrolyte, are also largely governed by the electrolyte formulation.[2d, 3] Collectively, the nature of the electrolyte is critical to the overall performance of the battery, including rate capability, durability and safety.[1-2, 4]

Electrolyte modulation has been widely adopted to optimize battery performance, which is facile and straightforward compared to other approaches. Early efforts concentrated on modifying electrolyte formulations[2d] by altering salt-solvent combinations[5] and applying functional additives[1, 6]. In recent years, the concentration regulation of electrolytes has made breakthroughs in both fundamental understanding and battery performance enhancement.[3b, 4d, 7] High-concentration electrolytes (HCE) are intensively exploited in both aqueous and organic systems.[4b, 8] The substantially altered ion solvation structure in HCE breeds a variety of unique bulk and interfacial features,[2b, 9] which benefit battery performance in many aspects, such as improving electrolyte stability at high voltages and forming more protective SEIs[10] for alloy and metal anodes. However, the high viscosity, low wettability and high cost of HCE greatly hinder their practical application.[2b] This conundrum is partly alleviated by forming "localized high concentration electrolytes (LHCE)",[11] which introduces non-solvating solvents as diluents in the HCE. In LHCE, the electrolyte presents a low concentration state macroscopically but maintains the unique solvation structure of HCE locally at the microscopic level.[12] However, increasing electrolyte concentration does not always guarantee an elevated battery performance. Recent studies has shown that the wide-temperature performance of Na-ion batteries,[7c] the rate performance of Li-S batteries,[13] and the cycling performance of Li metal batteries[5a, 14] are greatly enhanced in the low concentration electrolytes. These discrepant conclusions indicate the necessity for a more thorough exploration of the underlying principles for electrolyte concentration regulation.

The stability of the SEI contributes directly to the coulombic efficiency (CE) and continuance of the battery and is one of the most important criteria in electrolyte design.[2d, 4c, 4d, 8e, 8g, 15] However, among the many qualities of SEI, the orienting role of its mechanical properties in electrolyte regulation has rarely been reported. More drastic volume changes during charging and discharging increase the dependence of emerging metal batteries on the mechanical stability of SEI. Therefore, the power of the mechanical properties of SEI can be better elucidated using metal anode as the model system. K metal batteries have become a strong contender for large-scale energy storage due to their advantages in sustainability and cost[2c, 2d, 3b, 8d, 16]. Previous achievements in the stabilisation of K-metal anodes have mainly been achieved using three-dimensional porous collectors,[16a, 17] artificial SEI layers,[15a, 15b] or surface modification of potassium or copper plates,[18] and mostly in ether-based electrolytes[3b, 19]. In contrast, the progress with carbonate-based electrolytes is not satisfactory. Carbonate electrolytes, however, exhibit superior oxidative stability over ether ones, which is vital for achieving high energy density.[20] We have therefore investigated the fundamentals of optimizing K metal anode performance by adjusting the concentration of carbonate-based electrolyte. It is found that, despite the advantages of higher electrolyte concentrations (2 M) in the ionic conductivity, K metal using 0.5 M KFSI/ ethylene carbonate (EC) - diethyl carbonate (DEC) exhibits the best cycling performance due to the formation of mechanically stable SEI. These findings foreshadow the desirability of paying more attention to the mechanical properties of SEI, where low concentrations of carbonate electrolytes display merit.

2. Results and discussion

2.1 Concentration dependence of the physicochemical properties of electrolytes.

KFSI/EC-DEC (v:v=1:1) electrolytes at different concentrations from 0.25 to 2 M are prepared to investigate the variation pattern of their physicochemical properties. The viscosity of the electrolyte is found to grow with the content of KFSI due to the enhanced ion association (Figure S1).[7c] In addition, elevating the salt concentration ameliorates the ionic conductivity of the electrolyte (**Figure 1**a). As the salt concentration increases, this heightening becomes less pronounced as the high viscosity counteracts it.

2.2 The electrochemical performances of K metal batteries

The reversibility of the K plating-stripping process is investigated with different concentrations of KFSI/EC-DEC electrolytes in K/Cu half-cells, where Cu is adopted as the working electrode. The K deposition is carried out at 0.25, 0.5 and 1.0 mA cm^{-2} for one hour, and the stripping of K is terminated at 1 V (Figure 1b and Figure S2). The overpotential of K plating-stripping roughly declines with increasing electrolyte concentration. The ionic conductivity of both the electrolyte and SEI has an influence on the overpotential because they serially determine the barriers for ions to reach the metal surface and be reduced. In addition to the improved ionic conductivity of electrolyte by increasing the concentration, we also examined the concentration effect on the ionic conductivity of SEI by performing EIS tests (Figure. S3) on K/Cu cells. The results demonstrate the beneficial effect of high-concentration electrolytes in improving the electrode's kinetics. Surprisingly, no clear correlation is observed between the cycling performance of the K/Cu cell and its ionic conductivity. Under all tested current densities from 0.25 mA cm^{-2} to 1 mA cm^{-2} (Figure S2), Cu/K half cells demonstrate the best cycling performance in 0.5 M KFSI/EC-DEC electrolyte. The inset in Figure. 1b shows the average cycling data and standard error for multiple samples in four concentrations of electrolyte, with minimal dispersion found between samples tested in 0.5 M electrolyte. The CE values from the 10th cycle onwards are averaged for the cells with different concentration electrolytes and the results are plotted in Figure S4. Under all tested current densities, the value of CE in the 0.5 M electrolyte is the largest. A K plating-stripping efficiency of 97.5% is obtained at 1.0 mA cm^{-2} – 1.0 mAh cm^{-2}, among the best to date for K metal anodes in carbonate-based electrolytes (Table S1).

The impact of electrolyte concentration on battery performance is further explored in K/K symmetry cells. Figure 1c shows typical voltage profiles at a constant charge and discharge capacity of 0.5 mAh cm^{-2}. Similar to the case of K/Cu cell, K/K cell using the 0.5 M electrolyte exhibits the most stable cycling performance, with a cycle life of more than 500 hours. In contrast, the cycle life of K/K cells under the same test condition is only 160 hours, 250 hours and 30 hours in 0.25 M, 1 M and 2 M electrolytes, respectively (Figure 1c). The rate performances of K/K symmetry cells are provided in Figure S5. At low current densities, the overpotential is significantly lower in the high concentration electrolyte. As the current density progressively rises to 2.5 mA cm^{-2}, the dependence of overpotential on electrolyte concentration becomes less pronounced (Figure S5). The excellent rate performance of K/K cell in 0.5 M electrolyte should be attributed to its extremely stable SEI, because it has no advantage in viscosity or ionic conductivity compared to other concentrations of electrolyte. To verify this argument, we first cycle a K/K cell 20 times in 0.5 M electrolyte to form a stable SEI. Then the battery is disassembled, and the working and counter electrodes are washed carefully and assembled into a new cell using a fresh 0.25 M electrolyte. The cycle performance of the modified K/K battery is significantly improved, with the cycle life increased from 160 hours to 370 hours (Figure S6). At increased current density (2 mA cm^{-2}, Figure. S7) or capacity density (2 mAh cm^{-2}, Figure. S8), K/K batteries in 0.5 M KFSI/EC-DEC electrolyte all demonstrate superior cycling performances (Table S2). The full K-metal battery is assembled by using $K_xMnFe(CN)_6$ as the cathode material and K foil as the anode. Figure. S9 shows the cycling performance of the $K/K_xMnFe(CN)_6$ cells in different concentrations of KFSI/EC-DEC electrolytes. Compared to normal concentration (1M), the cell shows negligible increase in the polarization under 0.5 M electrolyte without sacrificing the stability of the cathode. The results indicate the low concentration electrolyte is fully compatible with the cathode while improving the stability of K metal anodes. .

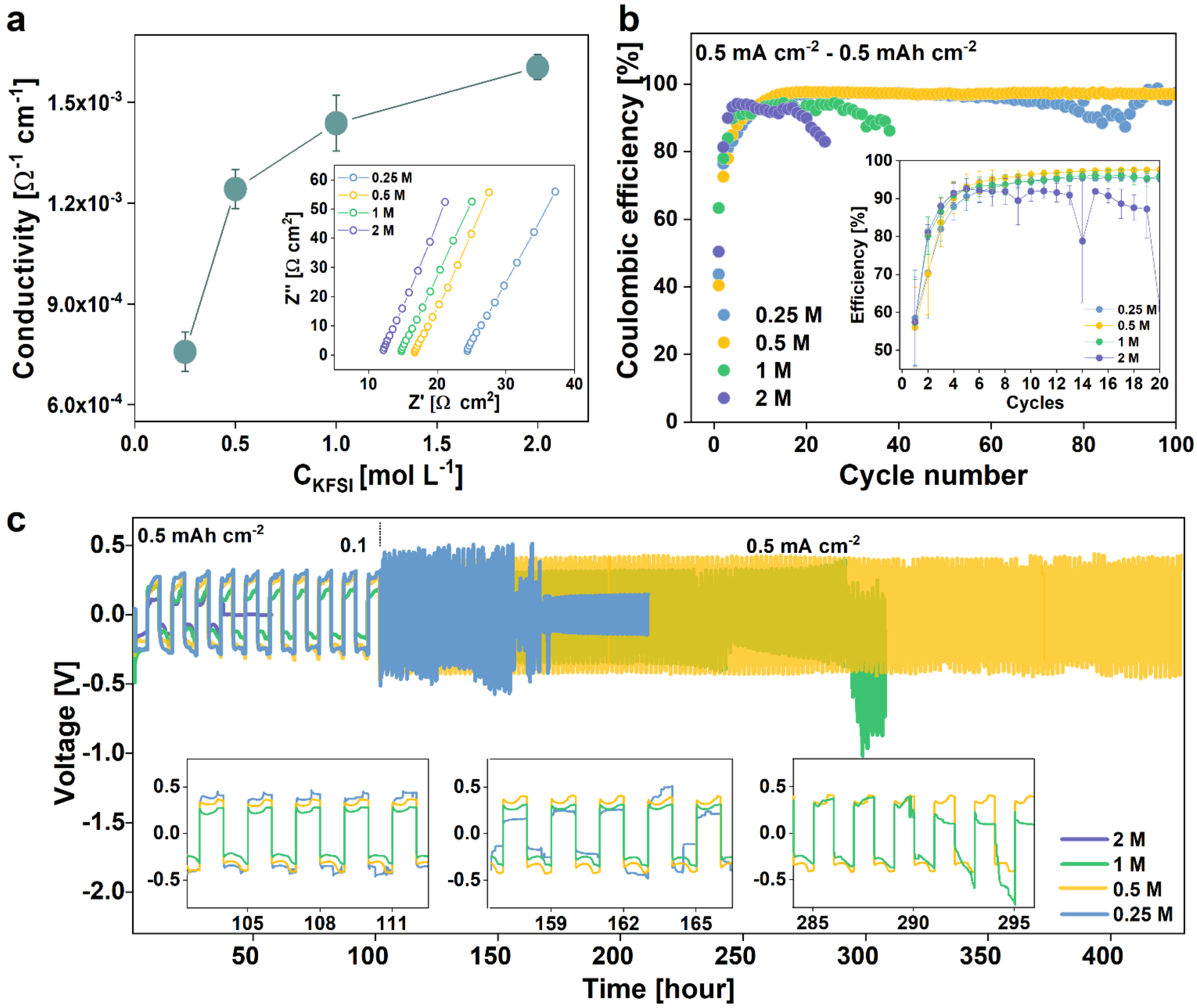

Figure 1. (The electrochemical performances of K metal batteries. **a** Concentration dependence of electrolyte ionic conductivity at 25 ℃ for KFSI/EC-DEC electrolyte. **b** K platting and stripping efficiencies on the Cu foil under different concentrations of electrolytes at the rate of 0.5 mA cm^{-2} for 0.5 mAh cm^{-2} The inset shows the average coulombic efficiency and standard error of the K/Cu half-cells in these four concentrations of electrolyte. **c** Galvanostatic cycling of K/K symmetry cell in 0.25 M, 0.5 M, 1 M and 2 M KFSI/EC-DEC electrolytes at 0.5 mA cm^{-2} – 0.5 mAh cm^{-2} after pre-cycling at 0.1 mA cm^{-2} – 0.5 mAh cm^{-2} for 10 cycles..)

2.3 K plating morphologies

Figure 2 shows the three-dimensional (3D) morphology of the K anode after 10 cycles in four different concentrations of electrolyte. The brightness of the colours in the 3D image represents the height of the position. Samples with approximate colour at each location have the most uniform deposition surface. To quantify the surface roughness of the K anode after discharge, five non-overlapping areas of around 25 μm^2 are randomly selected for each sample to calculate their Ra, and the average values are provided in Figure 2. Ra is the arithmetic average of the absolute values of the surface height deviations measured from the mean plane. The deposition surface of K in 0.5 M electrolyte has the smallest value of Ra, followed by 1 M, 0.25 M, and 2 M. To better visualize the differences in roughness, we select two positions (labelled A-A' and B-B') in each of the 3D images and plot their corresponding cross-sectional height profiles in Figure 2. From the 3D morphology photos, roughness data, and cross-sectional profiles, K has the most homogeneous platting behaviour in the 0.5 M electrolyte. This is consistent with the fact that K/Cu and K/K cells using the 0.5 M electrolyte have the best cycle stability. We also verify the phenomenon by SEM, which shows the most homogeneous morphology of K metal anode after cycling in 0.5 M electrolyte.

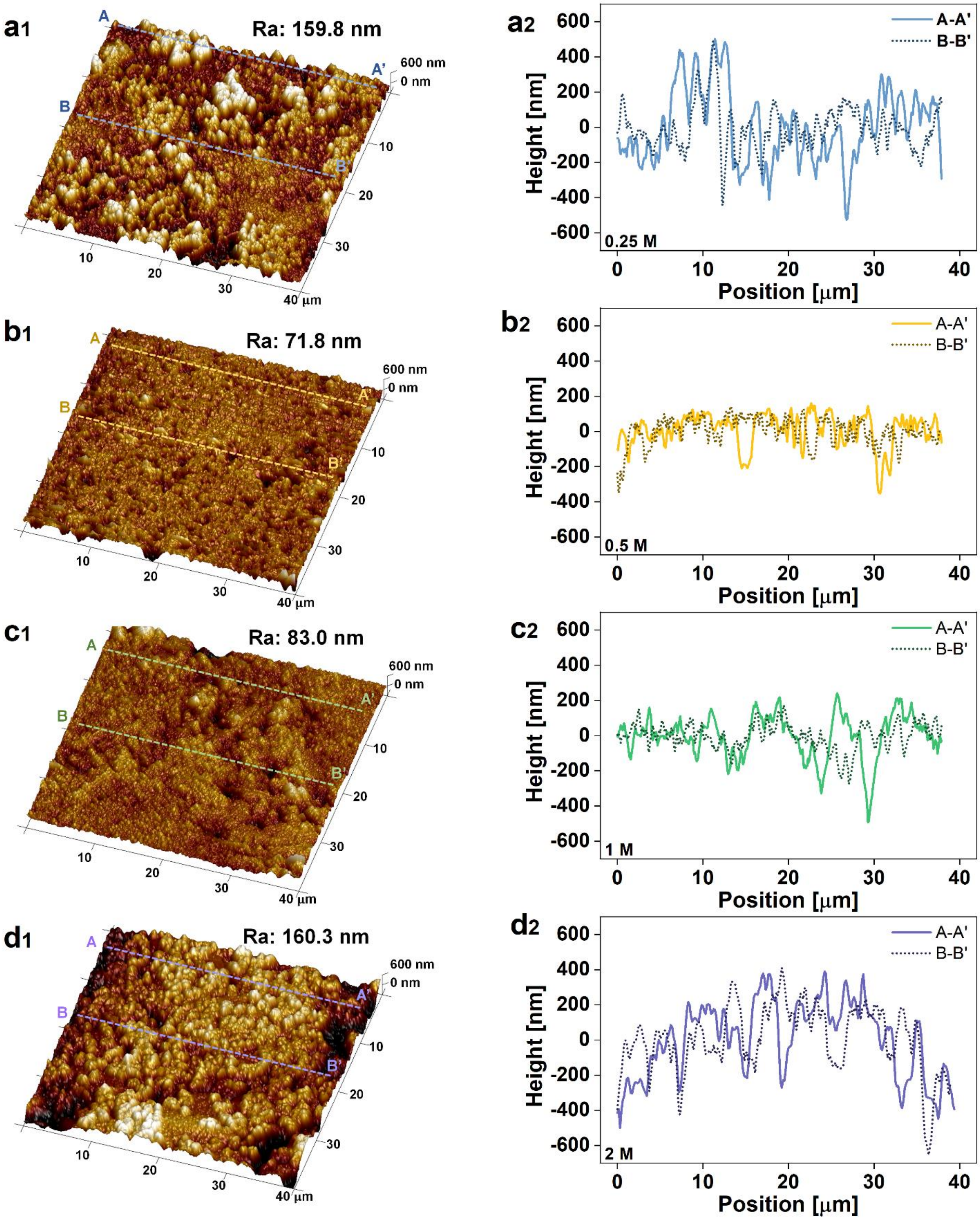
a1
Ra: 159.8 nm
A
A'
B
B'
600 nm
0 nm
10
20
30
40 μm
a2
A-A'
B-B'
Height [nm]
Position [μm]
0.25 M
b1
Ra: 71.8 nm
b2
0.5 M
c1
Ra: 83.0 nm
c2
1 M
d1
Ra: 160.3 nm
d2
2 M
600
400
200
0
-200
-400
-600

Figure 2. (K plating morphologies. The 3D topography images and the sectional height profiles of K anode surface after 10 cycles in **a** 0.25 M, **b** 0.5 M, **c** 1 M and **d** 2 M KFSI/EC-DEC electrolytes.)

2.4 Mechanical properties of SEI

The distinct deposition morphologies of K may arise from the variations in the mechanical properties of SEI. The two mechanical properties most used to characterize the adaptability of SEI to deformation are Young's modulus (E) and the elastic strain limit (ε_Y). E is primarily an indication of the SEI's ability to resist deformation; the higher the E, the greater the external force required to cause the same level of deformation. The elastic strain limit ε_Y is the maximum amount of deformation that can be achieved before irreversible deformation of the SEI occurs. Two consecutive AFM-based nanoindentation tests are carried out at the same position of SEI to evaluate Young's modulus (E) and the elastic strain limit (ε_{Y}) of the SEI. A small force is applied to elastically deform the SEI firstly, and then a large force is used to intentionally break the SEI.[21] The electrodes are charged/discharged for ten cycles to reach a steady state before AFM tests. For each electrode sample, over 100 test positions are collected. **Figure 3**a, b presents the histogram and the peak value of the distribution curve (lognormal) of E and ε_{Y} for SEIs formed in different concentrations of electrolyte, respectively. As the electrolyte concentration increases, the SEI displays an increment in E and a reduction in ε_{Y}. The ideal SEI would like to have both a large E and a large ε_{Y}, but as the results in Figure. 3 show, materials with a larger E tend to have a smaller ε_{Y}, while materials with a larger ε_{Y} tend to be less resistant to deformation. Considering that both E and ε_{Y} have an impact on the stability of SEI, an energy-based concept, i.e., the maximum elastic deformation energy ($U \propto E \cdot {\varepsilon_{\mathrm{Y}}}^5$, see the supplementary note 1 for the derivation),[21a] is adopted here to reflect the mechanical stability of SEI). The higher the value of U, the greater the amount of deformation energy that the SEI can reversibly absorb during the charge/discharge cycle. U is derived by assuming that the nonuniformly deposited K clusters indent the SEI locally under the battery's assembly pressure. The histogram of U are shown in Figure 3c. Interestingly, although the values of E and ε_Y of SEI vary continuously with the electrolyte concentration, the U-value combining the effects of E and ε_Y reaches a maximum in the 0.5 M electrolyte. At cycle 10, the *U* of SEI formed in 0.25 M, 1 M and 2 M electrolytes is 84.64%, 64.15% and 61.46% of that in 0.5 M electrolyte, respectively.

The dynamic evolution of SEI properties as the cycle proceeds is also of paramount importance for the cycling stability of the battery. Therefore, we characterized the SEI's mechanical properties after 45 cycles, and the corresponding *U*-values are shown in Figure 3d. It is worth noting that the *U*-value of SEI formed in the 2 M electrolyte is too low and the battery fails to last 45 cycles. By cycle 45, the *U* of SEI in 0.25 M and 1 M electrolytes is 86.86% and 28.91% of the SEI in 0.5 M electrolyte, respectively. Among the four concentrations, the SEI formed in 0.5 M electrolyte has distinct advantages, both in terms of the absolute value and the retention rate of *U*. ~~The cycling performances before the batteries are disassembled for mechanical tests are provided in Figure. S12.~~

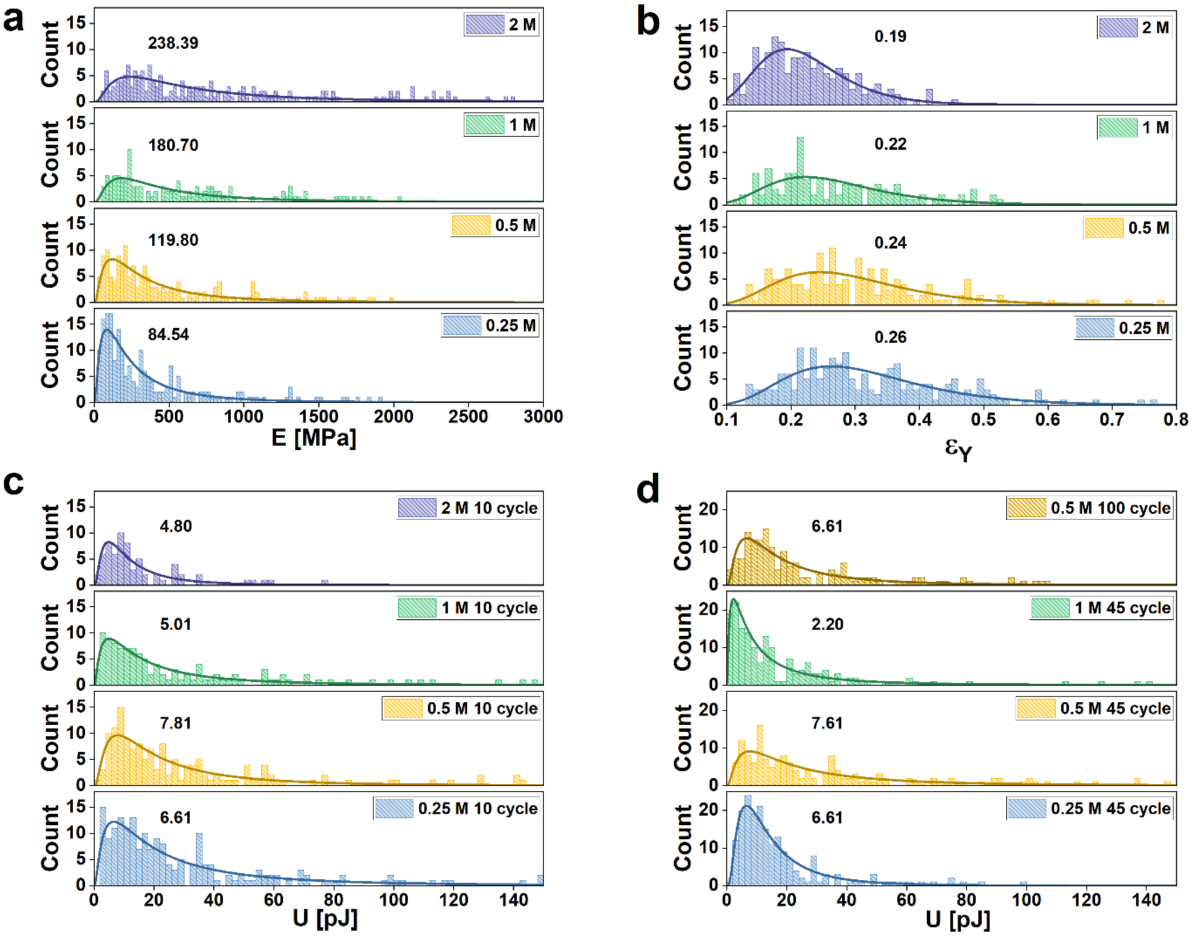

Figure 3. (Mechanical Properties of SEI. The histograms with the peak value of the distribution curve for **a** Young's modulus after 10 cycles, **b** elastic strain limit after 10 cycles, **c** the maximum

elastic deformation energy of SEI after 10 cycles and **d** the maximum elastic deformation energy of SEI after 45 cycles ~~and 100 cycles~~)

2.5 Chemical composition of SEI

To explore the origin of the concentration dependence on the properties of SEI, the chemical composition of SEI is analysed by X-ray photoelectron spectroscopy (XPS). The peak positions and combinations in **Figure 4**a-d indicate that the SEIs formed in different concentrations of KFSI/EC-DEC electrolyte have similar characteristics in chemical composition. The C-C/C=C (284.78 eV), C-O (286.91 eV), C=O (288.05 eV) in C 1s spectra (Figure 4a) and the C-O (532.14 eV) and C=O (531.1 eV) in O 1s (Figure 4b) spectra are organic decomposition products of EC or DEC.[22] The K-F (685.30, 683.41 eV) and S-F (687. 66 eV) peaks in F 1s spectra (Figure 4c) and the $KHSO_4$/KFSI (169.89 eV), K_2SO_4 (168.64 eV) and K_2SO_3 (166.76 eV) peaks in S 2p spectra originate mainly from the decomposition of KFSI and all become more intense as the electrolyte concentration increases.[8a, 22a] As shown in Figure 4e, the carbon content of the SEI increases from 70.5 at.% to 84.9 at.% as the KFSI concentration decreases from 2 M to 0.25 M.[8a] Such high carbon contents indicate that the SEIs formed in the four concentrations of KFSI/EC-DEC electrolyte are all dominated by organic components. With the increasing concentration of KFSI, an increment in the inorganic component content is verified in the percentages of inorganic matter in the SEI (Figure 4f) and is also reflected in the percentage of elements like N, F, S, K (Figure 4e). These results indicate that high concentration electrolytes aggravate the decomposition of KFSI.[8a, 22a]

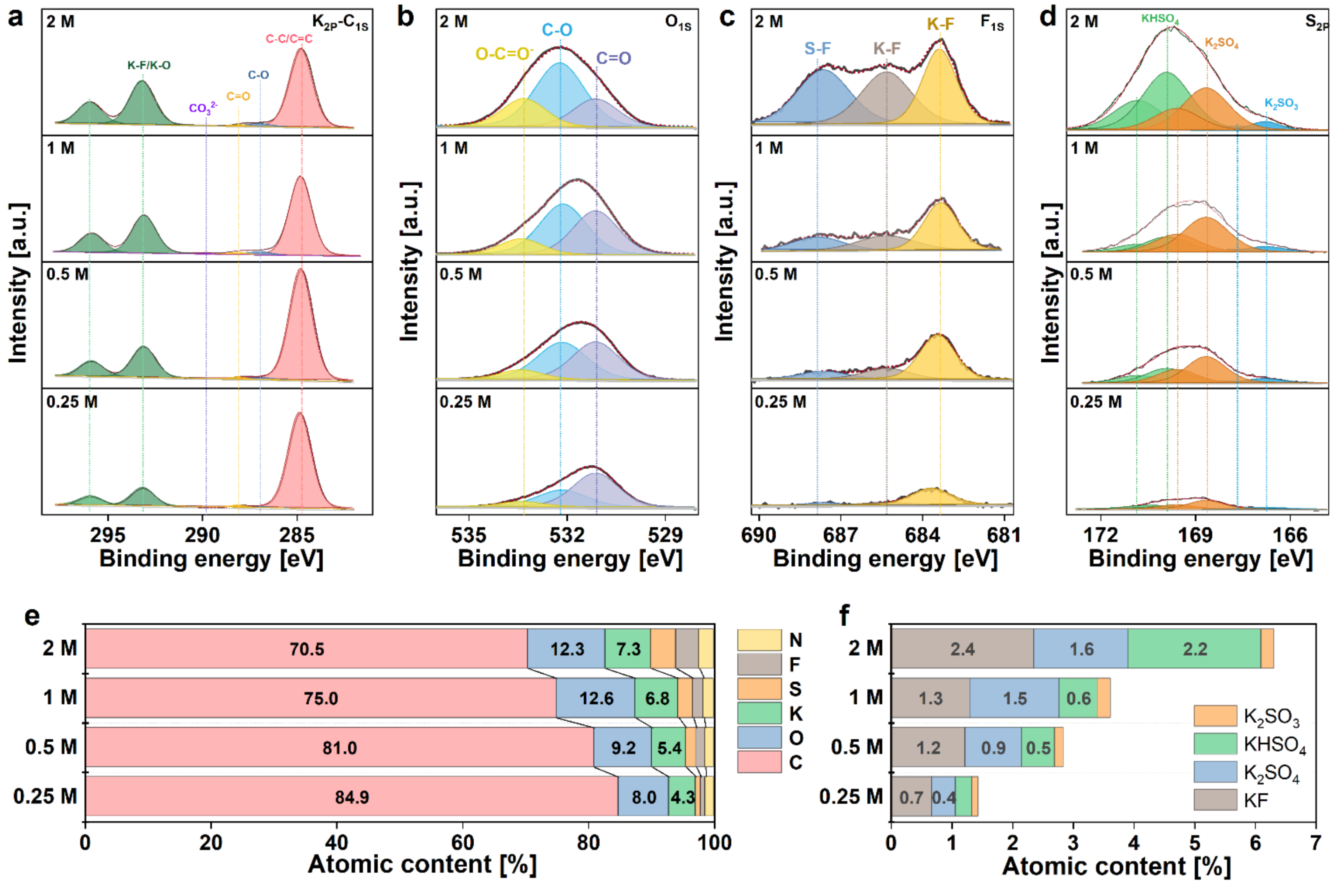

Figure 4. (Chemical compositions of SEI. XPS spectra of a K 2p and C 1s, b O 1s, c F 1s, and d S 2p peaks of the K metal anode cycled in 0.25 M, 0.5 M, 1 M and 2 M KFSI/EC-DEC. The calculated percent composition of e elements and f inorganic salts in SEI.)

2.6 The structure-property relationship of SEI

The microstructure of SEI formed in KFSI/EC-DEC electrolytes are further characterized using the cryo-TEM method. The obtained HRTEM, HAADF-STEM and SAED images (Figure S12) indicate a composite structure of SEI with crystalline inorganic particles embed in an amorphous matrix. In combination with previous information on the chemical composition and mechanical properties of the SEI obtained by XPS and AFM, we postulate that the SEI formed on the K metal anode in the KFSI/EC-DEC electrolyte has the structure of a polymer-based inorganic particle-filled composite (**Figure 5**). This structure accounts well for the concentration dependences of the ionic conductivity, Young's modulus, elastic strain limit of SEI and the K deposition morphology: 1) The increased amount of inorganic species, especial KF, potentially benefits the ionic conductivity, similar to the LiF-rich SEI in Li-ion batteries.[23] As a result, the ionic impedance of SEI formed in highly concentrated electrolytes is relatively low. 2) For polymer matrix composites reinforced with inorganic particles, the apparent Young's modulus of the material increases with the content of the inorganic reinforcements.[24] The increase in the inorganic content also means an increase in the mechanically weak intermediate phase, which will reduce the elastic strain limit of the composite. To investigate whether this conclusion applies to the case of SEI deformation and to elucidate the variation pattern of the elastic deformation energy of SEI, we have conducted a finite element simulation (see the supplementary note 2 for the details) for the mechanical properties of SEI with this composite structure. The simulation results (Figure S14-S16 show that the Young's modulus of the SEI increases and the elastic strain limit decreases as the number of inorganic particles increases, while the maximum elastic deformation energy reaches a maximum at moderate content of inorganic particles. 3) The SEI with a low Young's modulus provides less resistance to the growth of K particles, resulting in a rough deposited surface (Figure 5a and Figure 2a). 4) The SEI with a high Young’s modulus and a low elastic strain limit is not easily deformed and will compress the outward growth of K to some extent.[25] However, due to the weak mechanical properties of the interface between the inorganic contents and the organic matrix, the SEI is prone to cracking during cycling (Figure S17, Figure 5c).[26]

2.7 Theoretical simulations on the action mechanism of mechanical properties of SEI

Finite element simulations (FEM) are carried out to elucidate the influence of the mechanical properties of SEI on the plating behaviour of potassium. Three models corresponding to the 0.25 M, 0.5 M and 2 M KFSI/EC-DEC systems are specifically constructed (Figure S8). The conductivity of the electrolyte and SEI of the three models are based on the values obtained before (Figure 1a and Figure S4b). The deposition morphologies of potassium are established as follows: (a) the SEI formed in the 0.25 M electrolyte has a lower Young's modulus and is less resistant to the growth of potassium, thus leading to rapidly growing potassium clusters in the vertical direction (Figure 5a and Figure S8a); (b) the large Young's modulus of the SEI formed in the 2 M electrolyte presents a significant resistance to potassium growth, reducing the growth rate of potassium in the vertical direction and promoting potassium growth in the horizontal direction. Nevertheless, its small yield strain limit makes the SEI susceptible to cracking under the interactions with the potassium clusters (Figure 5c and Figure S8c); (c) in the 0.5 M electrolyte, the deposition pattern of potassium lies between the cases of 0.25 M and 2 M electrolytes (Figure 5b and Figure S8b). The meshing methods for these three models are provided in Figure S9. The potential difference between the upper and lower boundaries of the FEM model was set to 0.1 V.

Figure 5d-f show the simulation results of the electric field strength for different models, and the corresponding electric potential distribution is presented in Figure S10. Among the three systems, the most uniform electric field is realized under 0.5 M electrolyte, reducing the risk of dendrite growth. Turning to 0.25 M case, the surfaces of the potassium islands have the same potential due to the high electrical conductivity of potassium. Since the electric field corresponds to the varying gradient of voltage, the electric field strength is zero between adjacent vertically growing potassium (Figure 5d). These simulation results well explain the dendrite growth phenomenon on metal anodes: driven by the heterogeneous electric field, subsequent potassium is deposited preferentially on top of the previously grown potassium clusters rather than in the regions between them. For the case of the 2 M electrolyte, an obvious electric field enhancement occurs at the crack position of the SEI (Figure 5f). This will lead to preferential deposition of potassium below the crack, exacerbating the inhomogeneity of the deposited surface, which in turn triggers dendrite growth. These results provide a more explicit understanding of the mechanism by which the mechanical properties of SEI contribute to the cycling performance of alkaline metal anodes and will contribute significantly to the establishment of structure-property-function relationships for SEI.

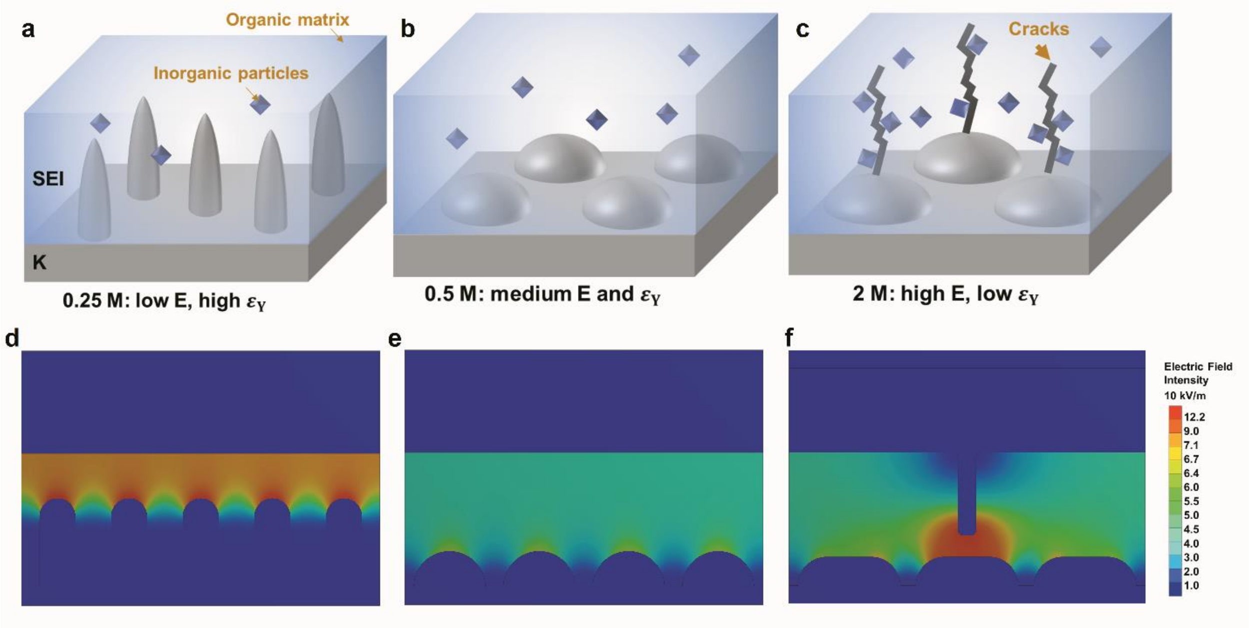

Figure 5. (Theoretical models and simulation results on the structure-property-function relationships of SEI. Illustrations of inorganic-organic SEIs (top), and the simulation results of electric field (bottom) in KFSI/EC-DEC electrolytes with concentrations of **a, d** 0.25 M, **b, e** 0.5 M and **c, f** 2 M electrolyte systems.)

One point to mention is that the relationship between electrolyte concentration and cell performance that we observed in the KFSI/EC-DEC system does not apply to all electrolyte systems. For example, in many electrolyte systems (e.g. 2 M KFSI/triethyl phosphate (TEP),[4d] 4 M KFSI/diethylene glycol dimethyl ether (DEGDME),[8a] 1 M[3b], 3 M[22c] and 5 M[3b] KFSI/dimethoxyethane (DME), and 2.3 M KFSI+50 mM KNO_3/DME[8g]) the performance of the cell increases with increasing electrolyte concentration. The discrepancy in these experimental results stems from the fact that SEI has a different microstructure. For instance, the SEIs in the KFSI/DME and KFSI/DEGDME are all reported to form an almost single-phase, highly homogeneous SEI with no directly visible second phase present in the HRTEM images. The possible reason is that the inorganic components are uniformly dispersed in the organic matrix with ultra-small particle sizes and no significant interphases are produced. Consequently, as the inorganic salt content of SEI increases with the concentration of electrolyte, the Young's modulus of SEI is increased, but the elastic deformation limit of SEI is not appreciably reduced as no stress concentration is induced. Similarly, for SEIs with a bilayer structure, there will be a different relationship between composition and properties. These phenomena indicate that each electrolyte system is unique and that a complete chain of composition-structure-performance relationships is necessary to accurately grasp the operation of a battery in a particular electrolyte. In this work, we focus on the most common carbonate electrolyte that has been commercialized in Li-ion batteries for facilitating the practical application.

3. Conclusion

To probe the importance of mechanical properties of SEI in electrolyte design, a series of K metal anodes with regular variations in physicochemical properties of electrolyte and SEI were constructed by varying the concentration of KFSI/EC-DEC electrolytes. The high concentration increases the ionic conductivity of the electrolyte and the resulted SEI, both of which are beneficial to decreasing the overpotential during K plating/stripping. Despite these, increasing the concentration does not benefit the CE and cycle life. A smooth K plating morphology is observed in the electrolyte with a low concentration of 0.5 M KFSI/EC-DEC, resulting in the highest CE and longest cycle time. We reveal such an unusual stability root in the alternation of SEI's nanostructure. As the electrolyte concentration increases from 0.25 M to 2 M, the content of inorganic components in the organic-dominated SEI gradually increases. This leads to an increase in Young's modulus and a decrease in the elastic strain limit. As a combined consequence of varied E and ε_Y, the SEI formed in the 0.5 M KFSI/EC-DEC electrolyte has the largest reversible elastic deformation energy (U) to accommodate the deformation during K plating. Finite element simulations show that the SEI with significant drawback in either E or ε_Y inevitably triggers dendritic growth of potassium, which explains the poor cycling performance of potassium metal anodes in 0.25 M and 2 M electrolytes. These results demonstrate that the mechanical properties of SEI play a dominant role in determining the cycling performance of metal anodes in carbonate electrolytes and should be emphasized in the electrolyte design. It also suggests that there is plenty of room at the low concentration in optimizing the electrode/electrolyte interface in parallel to the high concentration.

4. Experimental Section

Electrolyte: Electrolytes were prepared by dissolving the salt KFSI (Fute Chemical, purity 98%) into the solvents EC (DoDochem, purity 99.95%)-DEC (DoDochem, purity 99.95%) with the volume ratio being 1:1 at concentrations of 0.25 M, 0.5 M, 1 M, and 2 M.

Cathode: The $K_xMnFe(CN)_6$ cathode was prepared by precipitation in aqueous solution *[ref]*. Solution A was obtained by adding 50 wt.% Manganese (II) nitrate solution ($Mn(NO_3)_2$ solution, 2.3g) into 50 mL DI water. Solution B was obtained by dissolve Potassium ferrocyanide ($K_4[Fe(CN)_6]\cdot 3H_2O$, 1.27 g) and potassium chloride (KCl, 17.8 g) into 100 mL DI water. Solution A is added dropwise to solution B under magnetic stirring. After aging for 2 hours, the precipitate was collected by centrifugation and dried under vacuum at 60 °C.

Battery assembly: All batteries were assembled with the two-electrode CR2032 coin half-cell in an argon-filled glovebox (H_2O<0.1 ppm, O_2<0.1 ppm). The K electrode was prepared by pressing K metal (>98%, Sigma-Aldrich) into circular sheets (1.13 cm^2 in surface area and ~1 mm in thickness). The K/K symmetry cells were assembled with two K electrodes. The K/Cu half cells were assembled with a K electrode and a bare Cu foil (diameter: 12 mm) working electrode. The separator consisted of a piece of Celgard-2320 (polypropylene-polyethylenepolypropylene) and a piece of glass fiber (Whatman, GF/D). 80 μL of electrolyte was used for each coin cell. Two stainless plates are adopted for each coin cell and the assemble pressure was set as around 5 MPa.

Electrochemical testing: The galvanostatic discharge/charge tests of K/K and K/Cu coin cells were conducted at a constant temperature of 25 ℃. The charge cutoff voltage of K/Cu cell is 1.0 V (vs. K^+/K). The CE was defined as the ratio of K stripping to that plating on the Cu substrate. The electrochemical impedance spectroscopy (EIS) spectra were conducted at the open circuit potential with a frequency ranging from 100 kHz to 0.01 Hz with a perturbation voltage amplitude of 5 mV. The ionic conductivity of the electrolyte was measured by EIS testing in a customized stainless steel cell using polished stainless steel (SS316L) plates as the two electrodes.[27] The conductivity κ was deduced from the equation: $\kappa = d/(R \cdot A)$,[27] where d is the distance between the two electrodes, R is the measured resistance, and A is the surface area of the electrodes.

Materials characterization: The viscosity of the electrolyte was measured with an Ubbelohde viscometer. Morphological observations were conducted on the atomic force microscopy. The chemical composition of the SEI was characterized by X-ray photoelectron spectroscopy. The obtained XPS data was calibrated with respect to the C-C speak at 284.8 eV in C 1s spectrum. All coin cells were disassembled in the argon glove box and the potassium electrodes to be characterized were washed by the dimethyl carbonate (DMC, DoDochem, purity 99.95%) several times and dried in the glove box.

AFM-based nanoindentation test of SEI: The mechanical characterization of SEI was carried out by an AFM in a glove box. An probe with a spring constant of 20.16 N m^{-1} was used. Prior to each test, the deflection sensitivity of the AFM cantilever was calibrated on a clean sapphire sample. The tip radius (R) was calibrated using a reference sample with a known modulus of elasticity. The tip radius and spring constant were calibrated before and after each indentation test to ensure the accuracy of the data analysis. A scan of the test area was first performed with an ultra-low setting force of 2 nN to portray the surface morphology with no damages introduced to the sample. More than 100 positions were selected in the scanning area using the "point-and-shoot" function of the AFM. Adjacent test positions were separated by a minimum of 300 nm to avoid mutual interference. For the first test, the maximum force was set at 30 nN to obtain the elastic deformation behavior of SEI. The maximum loading force was set to 900 nN in the second test to deliberately break the SEI in order to obtain information on its elastic strain limit.

Finite element method simulations: We used the Ansys electrical conduction model to simulate the effect of the mechanical properties of SEI on the deposition behavior of potassium. Three models corresponding to the 0.25 M, 0.5 M and 2 M KFSI/EC-DEC systems were constructed. Details of the dimensions of the models are shown in Figure S9. These models were built to simulate the electric field distribution in a half-cell after the formation of the initial deposition morphology of potassium. The cathode (potassium, resistivity: 7.2×10^{-8} ohm m) was modelled with a smooth plate. In the presence of SEIs with different mechanical properties, the potassium initially deposited at the anode has different topography, and therefore, the anode was modelled as potassium islands with different profiles. Between the cathode and anode were the electrolyte and SEI layers. The resistivity values of the electrolyte and SEI were first set to 6.3×10^{4} ohm·m and 7.9×10^{6} ohm·m, respectively, and were the same for all three models. The meshing grid was constructed using three-node elements whose dimensions were controlled to 0.05 μm (Figure S10). The potential difference between the cathode and anode was set to 0.1 V.

Supporting Information

Supporting Information is available from the Wiley Online Library or from the author.

Acknowledgements

This work was supported by the General Research Fund (GRF) scheme of the Hong Kong Research Grants Council [Projects No. 15301220], the Hong Kong Polytechnic University (ZVGH, ZVRP), and Guangdong-Hong Kong-Macau Joint Laboratory [grant no. 2019B121205001].

Data availability:

The data that support the findings of this study are available from the corresponding author upon reasonable request.

CRediT authorship contribution statement

Yao Gao: Conceptualization, Methodology, Validation, Formal analysis, Investigation, Visualization, Writing – original draft, Writing – review & editing. **Zhen Hou:** Methodology, Writing – review & editing. **Rui Zhou**: Methodology, Writing – review & editing. **Biao Zhang:** Conceptualization, Methodology, Resources, Supervision, Writing – review & editing, Project administration, Funding acquisition.

Conflicts of interest

There are no conflicts to declare.

References:

[1] Y.-S. Hu, Y. Lu, *ACS Energy Letters* **2020**, *5*, 3633-3636.

[2] aO. Borodin, J. Self, K. A. Persson, C. Wang, K. Xu, *Joule* **2020**, *4*, 69-100; bM. Li, C. Wang, Z. Chen, K. Xu, J. Lu, *Chem. Rev.* **2020**, *120*, 6783-6819; cP. Liu, D. Mitlin, *Acc. Chem. Res.* **2020**, *53*, 1161-1175; dH. Wang, D. Yu, X. Wang, Z. Niu, M. Chen, L. Cheng, W. Zhou, L. Guo, *Angew. Chem. Int. Ed.* **2019**, *58*, 16451-16455.

[3] aG. Yang, S. Frisco, R. Tao, N. Philip, T. H. Bennett, C. Stetson, J.-G. Zhang, S.-D. Han, G. Teeter, S. P. Harvey, *ACS Energy Letters* **2021**, *6*, 1684-1693; bN. Xiao, W. D. McCulloch, Y. Wu, *JACS* **2017**, *139*, 9475-9478; cW. Liu, P. C. Liu, D. Mitlin, *Advanced Energy Materials* **2020**, *10*.

[4] aX.-B. Cheng, R. Zhang, C.-Z. Zhao, Q. Zhang, *Chem. Rev.* **2017**, *117*, 10403-10473; bJ. Touja, P. N. Le Pham, N. Louvain, L. Monconduit, L. Stievano, *Chem. Commun.* **2020**, *56*, 14673-14676; cH. Sun, P. Liang, G. Zhu, W. H. Hung, Y.-Y. Li, H.-C. Tai, C.-L. Huang, J. Li, Y. Meng, M. Angell, *Proceedings of the National Academy of Sciences* **2020**, *117*, 27847-27853; dS. Liu, J. Mao, Q. Zhang, Z. Wang, W. K. Pang, L. Zhang, A. Du, V. Sencadas, W. Zhang, Z. Guo, *Angew. Chem. Int. Ed.* **2020**, *59*, 3638-3644.

[5] aH. Zheng, H. F. Xiang, F. Y. Jiang, Y. C. Liu, Y. Sun, X. Liang, Y. Z. Feng, Y. Yu, *Advanced Energy Materials* **2020**, *10*, 12; bY. F. Zhang, Y. R. Zhong, Z. S. Wu, B. Wang, S. Q. Liang, H. L. Wang, *Angew. Chem. Int. Ed.* **2020**, *59*, 7797-7802.

[6] aJ. M. Zheng, M. H. Engelhard, D. H. Mei, S. H. Jiao, B. J. Polzin, J. G. Zhang, W. Xu, *Nature Energy* **2017**, *2*, 8; bH. Zhang, G. G. Eshetu, X. Judez, C. M. Li, L. M. Rodriguez-Martinez, M. Armand, *Angew. Chem. Int. Ed.* **2018**, *57*, 15002-15027.

[7] aL. Suo, Y.-S. Hu, H. Li, M. Armand, L. Chen, *Nature Communications* **2013**, *4*, 1-9; bL. Suo, O. Borodin, T. Gao, M. Olguin, J. Ho, X. Fan, C. Luo, C. Wang, K. Xu, *Science* **2015**, *350*, 938-943; cY. Li, Y. Yang, Y. Lu, Q. Zhou, X. Qi, Q. Meng, X. Rong, L. Chen, Y.-S. Hu, *Acs Energy Letters* **2020**, *5*, 1156-1158.

[8] aW. Xu, H. Wang, J. Hu, H. Zhang, B. Zhang, F. Kang, D. Zhai, *Chem. Commun.* **2021**, *57*, 1034-1037; bP. Münster, A. Heckmann, R. Nölle, M. Winter, K. Beltrop, T. Placke, *Batteries* **2019**, *2*, 992-1006; cP. Liu, Y. Wang, H. Hao, S. Basu, X. Feng, Y. Xu, J. A. Boscoboinik, J. Nanda, J. Watt, D. Mitlin, *Adv. Mater.* **2020**, 2002908; dM. Ye, J. Y. Hwang, Y. K. Sun, *Acs Nano* **2019**, *13*, 9306-9314; eP. Liu, H. Hao, H. Celio, J. Cui, M. Ren, Y. Wang, H. Dong, A. R. Chowdhury, T. Hutter, F. A. Perras, *Adv. Mater.* **2021**, 2105855; fS. Wang, Y. Yan, D. Xiong, G. Li, Y. Wang, F. Chen, S. Chen, B. Tian, Y. Shi, *Angew. Chem. Int. Ed.* **2021**; gH. Wang, J. Dong, Q. Guo, W. Xu, H. Zhang, K. C. Lau, Y. Wei, J. Hu, D. Zhai, F. Kang, *Energy Storage Materials* **2021**, *42*, 526-532.

[9] aY. Yamada, J. Wang, S. Ko, E. Watanabe, A. Yamada, *Nature Energy* **2019**, *4*, 269-280; bV. A. Azov, K. S. Egorova, M. M. Seitkalieva, A. S. Kashin, V. P. Ananikov, *Chem. Soc. Rev.* **2018**, *47*, 1250-1284.

[10] Q. Peng, S. Zhang, H. Yang, B. Sheng, R. Xu, Q. Wang, Y. Yu, *ACS nano* **2020**, *14*, 6024-6033.

[11] S. Chae, W.-J. Kwak, K. S. Han, S. Li, M. H. Engelhard, J. Hu, C. Wang, X. Li, J.-G. Zhang, *ACS Energy Letters* **2021**, 387-394.

[12] aL. Qin, N. Xiao, J. Zheng, Y. Lei, D. Zhai, Y. Wu, *Advanced Energy Materials* **2019**, *9*, 1902618; bS. R. Chen, J. M. Zheng, D. H. Mei, K. S. Han, M. H. Engelhard, W. G. Zhao, W. Xu, J. Liu, J. G. Zhang, *Adv. Mater.* **2018**, *30*, 7; cJ. Zheng, S. Chen, W. Zhao, J. Song, M. H. Engelhard, J.-G. Zhang, *ACS Energy Letters* **2018**, *3*, 315-321.

[13] aR. Glaser, F. Wu, E. Register, M. Tolksdorf, B. Johnson, J. Ready, M. Sanghadasa, G. Yushin, *J. Electrochem. Soc.* **2020**, *167*, 100512; bF. Wu, F. Chu, G. A. Ferrero, M. Sevilla, A. B. Fuertes, O. Borodin, Y. Yu, G. Yushin, *Nano Lett.* **2020**, *20*, 5391-5399.

[14] D. E. Galvez-Aranda, J. M. Seminario, *The Journal of Physical Chemistry C* **2020**, *124*, 21919-21934.

[15] aH. W. Wang, J. Y. Hu, J. H. Dong, K. C. Lau, L. Qin, Y. Lei, B. H. Li, D. Y. Zhai, Y. Y. Wu, F. Y. Kang, *Advanced Energy Materials* **2019**, *9*; bP. Shi, S. Zhang, G. Lu, L. Wang, Y. Jiang, F. Liu, Y. Yao, H. Yang, M. Ma, S. Ye, *Advanced Energy Materials* **2021**, *11*, 2003381; cP. Hundekar, S. Basu, X. L. Fan, L. Li, A. Yoshimura, T. Gupta, V. Sarbada, A. Lakhnot, R. Jain, S. Narayanan, Y. F. Shi, C. S. Wang, N. Koratkar, *Proc. Natl. Acad. Sci. U.S.A.* **2020**, *117*, 5588-5594; dY. Gu, W.-W. Wang, Y.-J. Li, Q.-H. Wu, S. Tang, J.-W. Yan, M.-S. Zheng, D.-Y. Wu, C.-H. Fan, W.-Q. Hu, *Nature communications* **2018**, *9*, 1-9; eW. Zhang, W. K. Pang, V. Sencadas, Z. Guo, *Joule* **2018**, *2*, 1534-1547.

[16] aP. Liu, Y. Wang, Q. Gu, J. Nanda, J. Watt, D. Mitlin, *Adv. Mater.* **2020**, *32*, 1906735; bC. Wei, Y. Tao, H. Fei, Y. An, Y. Tian, J. Feng, Y. Qian, *Energy Storage Materials* **2020**; cJ.-Y. Hwang, S.-T. Myung, Y.-K. Sun, *Adv. Funct. Mater.* **2018**, *28*, 1802938.

[17] aY. Xie, J. Hu, Z. Han, H. Fan, J. Xu, Y. Lai, Z. Zhang, *Nano Research* **2020**, *13*, 3137-3141; bH. Shi, Y. Dong, S. Zheng, C. Dong, Z.-S. Wu, *Nanoscale Advances* **2020**, *2*, 4212-4219; cX. Tang, D. Zhou, P. Li, X. Guo, B. Sun, H. Liu, K. Yan, Y. Gogotsi, G. Wang, *Adv. Mater.* **2020**, *32*, 1906739; dL. Wang, H. Wang, M. Cheng, Y. Hong, M. Li,

H. Su, J. Sun, J. Wang, Y. Xu, *ACS Applied Energy Materials* **2021**; eM. Zhou, W. Qi, Z. Hu, M. Cheng, X. Zhao, P. Xiong, H. Su, M. Li, J. Hu, Y. Xu, *ACS Applied Materials Interfaces* **2021**, *13*, 17629-17638; fJ. Y. Wang, J. C. Yuan, C. H. Chen, L. L. Wang, Z. B. Zhai, Q. R. Fu, Y. Liu, L. Dong, W. Yan, A. J. Li, J. J. Zhang, *Nano Energy* **2020**, *75*; gL. Qin, Y. Lei, H. Wang, J. Dong, Y. Wu, D. Zhai, F. Kang, Y. Tao, Q. H. Yang, *Advanced Energy Materials* **2019**, *9*, 1901427; hF. Qiao, J. Meng, J. Wang, P. Wu, D. Xu, Q. An, X. Wang, L. Mai, *Journal of Materials Chemistry A* **2021**, *9*, 23046-23054; iZ. Wei, A. Wang, X. Guan, G. Li, Z. Yang, C. Huang, J. Zhang, L. Ren, J. Luo, X. Liu, *Energy Environmental Materials* **2021**; jX. Zhao, F. Chen, J. Liu, M. Cheng, H. Su, J. Liu, Y. Xu, *Journal of Materials Chemistry A* **2020**, *8*, 5671-5678.

[18] aH. Yang, F. He, M. Li, F. Huang, Z. Chen, P. Shi, F. Liu, Y. Jiang, L. He, M. Gu, *Adv. Mater.* **2021**, 2106353; bQ. Yang, Y. Ding, G. He, *Chem. Commun.* **2020**, *56*, 3512-3515; cY. Li, L. Zhang, S. Liu, X. Wang, D. Xie, X. Xia, C. Gu, J. Tu, *Nano Energy* **2019**, *62*, 367-375.

[19] Z. Tai, Y. Li, Y. Liu, L. Zhao, Y. Ding, Z. Lu, Z. Peng, L. Meng, G. Yu, L. Liu, *Advanced Science* **2021**, *8*, 2101866.

[20] F. Ding, W. Xu, X. Chen, J. Zhang, M. H. Engelhard, Y. Zhang, B. R. Johnson, J. V. Crum, T. A. Blake, X. Liu, *J. Electrochem. Soc.* **2013**, *160*, A1894.

[21] aY. Gao, X. Du, Z. Hou, X. Shen, Y.-W. Mai, J.-M. Tarascon, B. Zhang, *Joule* **2021**, *5*, 1860-1872; bY. Gao, S.-Q. Shi, T.-Y. Zhang, *Nanoscale* **2017**, *9*, 6033-6040.

[22] aB. Li, J. Zhao, Z. Zhang, C. Zhao, P. Sun, P. Bai, J. Yang, Z. Zhou, Y. Xu, *Adv. Funct. Mater.* **2019**, *29*, 1807137; bL. Fan, R. Ma, Q. Zhang, X. Jia, B. Lu, *Angew. Chem. Int. Ed.* **2019**, *58*, 10500-10505; cL. Fan, S. Chen, R. Ma, J. Wang, L. Wang, Q. Zhang, E. Zhang, Z. Liu, B. Lu, *Small* **2018**, *14*, 1801806.

[23] J. Chen, X. Fan, Q. Li, H. Yang, M. R. Khoshi, Y. Xu, S. Hwang, L. Chen, X. Ji, C. Yang, *Nature Energy* **2020**, *5*, 386-397.

[24] aS.-Y. Fu, X.-Q. Feng, B. Lauke, Y.-W. Mai, *Journal of Composites Part B: Engineering* **2008**, *39*, 933-961; bZ. K. Zhu, Y. Yang, J. Yin, Z. N. Qi, *J. Appl. Polym. Sci.* **1999**, *73*, 2977-2984; cM. Dekkers, D. Heikens, *J. Appl. Polym. Sci.* **1983**, *28*, 3809-3815; dS.-Y. Fu, B. Lauke, *Composites Part A: Applied Science Manufacturing* **1998**, *29*, 575-583; eF. Eirich, in *Applied polymer symposia, Vol. 39*, **1984**, pp. 93-102; fK. Radford, *Journal of Materials Science* **1971**, *6*, 1286-1291.

[25] aC. Monroe, J. Newman, *J. Electrochem. Soc.* **2005**, *152*, A396-A404; bS. Yu, R. D. Schmidt, R. Garcia-Mendez, E. Herbert, N. J. Dudney, J. B. Wolfenstine, J. Sakamoto, D. J. Siegel, *Chem. Mater.* **2016**, *28*, 197-206; cP. Barai, K. Higa, V. Srinivasan, *Phys. Chem. Chem. Phys.* **2017**, *19*, 20493-20505; dX. Shen, R. Zhang, X. Chen, X. B. Cheng, X. Li, Q. Zhang, *Advanced Energy Materials* **2020**, *10*, 1903645.

[26] aS. Yuan, S. Weng, F. Wang, X. Dong, Y. Wang, Z. Wang, C. Shen, J. L. Bao, X. Wang, Y. Xia, *Nano Energy* **2021**, *83*, 105847; bM. Tanaka, J. B. Hooper, D. Bedrov, *Acs Applied Energy Materials* **2018**, *1*, 1858-1863.

[27] N. Zhang, F. Cheng, Y. Liu, Q. Zhao, K. Lei, C. Chen, X. Liu, J. Chen, *JACS* **2016**, *138*, 12894-12901.